Comparison of Near-Surface Attenuation from Surface Array-Based Seismic Noise Data and Borehole Weak-Motion Recordings at the STIN Test Site in Northeastern Italy

Ilaria Dreossi[*1] and Stefano Parolai[1,2]

Abstract

Seismic wave attenuation and the related shear-wave quality factor (Q_S) in the near surface are crucial parameters for ground motion simulations and seismic hazard assessments. Although recent approaches developed to calculate Q_S from seismic noise acquired by surface arrays have been accepted for practice, additional testing and comparison of results estimated using various geophysical methods are still necessary to verify the reliability of such techniques. This work presents the results of an experiment conducted at the STIN site in northeastern Italy, which is equipped with a 100 m deep instrumented borehole. A seismic noise campaign was implemented by installing a temporary independent local surface array of seismological stations. The gathered data were used to initially estimate the shear-wave velocity (V_S) profile and frequency-dependent Rayleigh-wave attenuation, and subsequently determine the Q_S factor via a linearized inversion method. The study compares these findings with the V_S and Q_S values derived from analyzing weak-motion events recorded by two permanent seismic sensors positioned at the top and bottom of the well. The results confirm the potential of the inversion procedure used to obtain Q_S from local-scale seismic noise arrays as a promising approach for conducting attenuation studies at the local level in less geologically complex sites.

Introduction

The shear-wave quality factor (Q_S) in near-surface layers is a key parameter for seismic wave propagation studies and seismic hazard assessments. The definition of Q_S varies among scientific communities, that is, seismology, geophysics, and geotechnical engineering, and its estimation involves various techniques such as laboratory analyses and active- and passive-source seismological data (Parolai *et al.*, 2022). It is worth noting that estimating Q_S from empirical data is more challenging than assessing shear-wave velocity (V_S). This is probably due to the difficulty in accurately constraining attenuation from seismic data.

Common methodologies for obtaining Q_S include borehole investigations such as downhole (e.g., Koedel and Karl, 2020) and crosshole (e.g., Lai and Özcebe, 2016a,b) methods. Data analyses of earthquakes recorded by vertically installed borehole arrays have also been the subject of extensive research (e.g., Riga *et al.*, 2019). At the local scale, attempts have been made to extract Q_S using noninvasive active-source surface array-based site characterization methods such as spectral analysis of surface waves (SASW) (e.g., Badsar *et al.*, 2010) and multichannel analysis of seismic waves (MASW) (e.g., Aimar *et al.*, 2024), which are typically applied to estimate

1. National Institute of Oceanography and Applied Geophysics—OGS, Trieste, Italy, https://orcid.org/0000-0002-4552-7506 (ID); https://orcid.org/0000-0002-9084-7488 (SP); 2. Department of Mathematics and Geosciences, University of Trieste, Trieste, Italy

*Corresponding author: idreossi@ogs.it

V_S profiles. Whereas most works based on SASW and MASW consider the spatial decay of Rayleigh waves to estimate the damping ratio, Badsar *et al.* (2010) proposed operating in the wavenumber domain using SASW tests. Researchers also utilized seismic noise (passive-source) measurements in an array configuration (e.g., Boxberger *et al.*, 2017) to reach deeper Q_S investigations, as opposed to high-frequency acquisitions from SASW and MASW. The SASW/MASW and seismic noise methodologies offer various advantages over boreholes. First, they are cost effective. Second, they facilitate data acquisition in urban areas due to the ease of using portable instrumentations. Third, they can be applied ad hoc, without waiting for weak- or strong-motion events in areas.

Dreossi and Parolai (2022) improved the linear inversion procedure of Parolai (2014) for computing the 1D Q_S structure of the subsoil by eliminating the requirement for trial-and-error calibration of the inversion parameters. Instead of the least-squares algorithm used in the original inversion, they adopted the simultaneous algebraic reconstruction technique (SART) (Andersen and Kak, 1984). Their tests at two sites where Q_S values had been previously calculated, and their estimation of the 1D Q_S model at a new site using SART, yielded positive outcomes. Based on these premises, the purpose of this work is to compare the Q_S calculated with SART at the local scale from a temporary independent surface array of seismological stations deployed in the vicinity of a borehole, with the Q_S obtained by analyzing four weak-motion events recorded by seismometers installed inside the borehole. For this experiment, a 100 m deep well (station code: STIN) with two permanent top and bottom sensors was selected.

The STIN Site

The 100 m deep cased borehole (aka: STIN) near the "Sette Sorelle" draining plant is located in San Stino di Livenza municipality (northeast Italy) (Fig. 1). The STIN well was constructed within an agreement with the Veneto region to monitor the seismic activity in northeastern Italy for Civil Protection purposes as part of the *Sistema di Monitoraggio terrestre dell'Italia Nord Orientale* infrastructure (see Bragato *et al.*, 2021). The STIN borehole has been equipped with an accelerometer at a depth of 0.5 m and a velocimeter at 100 m depth since August 2018. Both sensors record data at 100 samples per second.

The STIN site is situated in the Venetian plain (inset of Fig. 1), which was formed as a result of alluvial system evolution corresponding to climate and sea-level fluctuations during the

Quaternary period (Fontana *et al.*, 2010). The Tagliamento river played a significant role in this region's geomorphology, creating an extensive megafan and numerous incised valleys in its distal reach (Ronchi *et al.*, 2021). The site is dominated by alluvial deposits, specifically flood plain and natural bank deposits (Fontana *et al.*, 2012). Silty materials, either consisting of silt, clayey silt, silty clay, or sandy silt, can be found and are sometimes accompanied by lenses of fine sands (Fontana *et al.*, 2012). Organic or peaty silt layers are also present (Fontana *et al.*, 2012). The water table fluctuates between 0 and 2 m depth.

The stratigraphy of the STIN borehole is primarily composed of fine sediments, while below the 0.1 m depth of backfill material. The drilling survey revealed a succession of clay, silt, and sand layers down to a depth of 35.5 m, followed by a peat layer from 35.5 to 38.2 m, and a silt layer from 38.2 to 40.3 m depth. Below that, at depths of 40.3 to 100.0 m, alternating bands of sand (sometimes of a certain thickness) and clay were observed. For the stratigraphy of the STIN well, see Table S1, available in the supplemental material to this article.
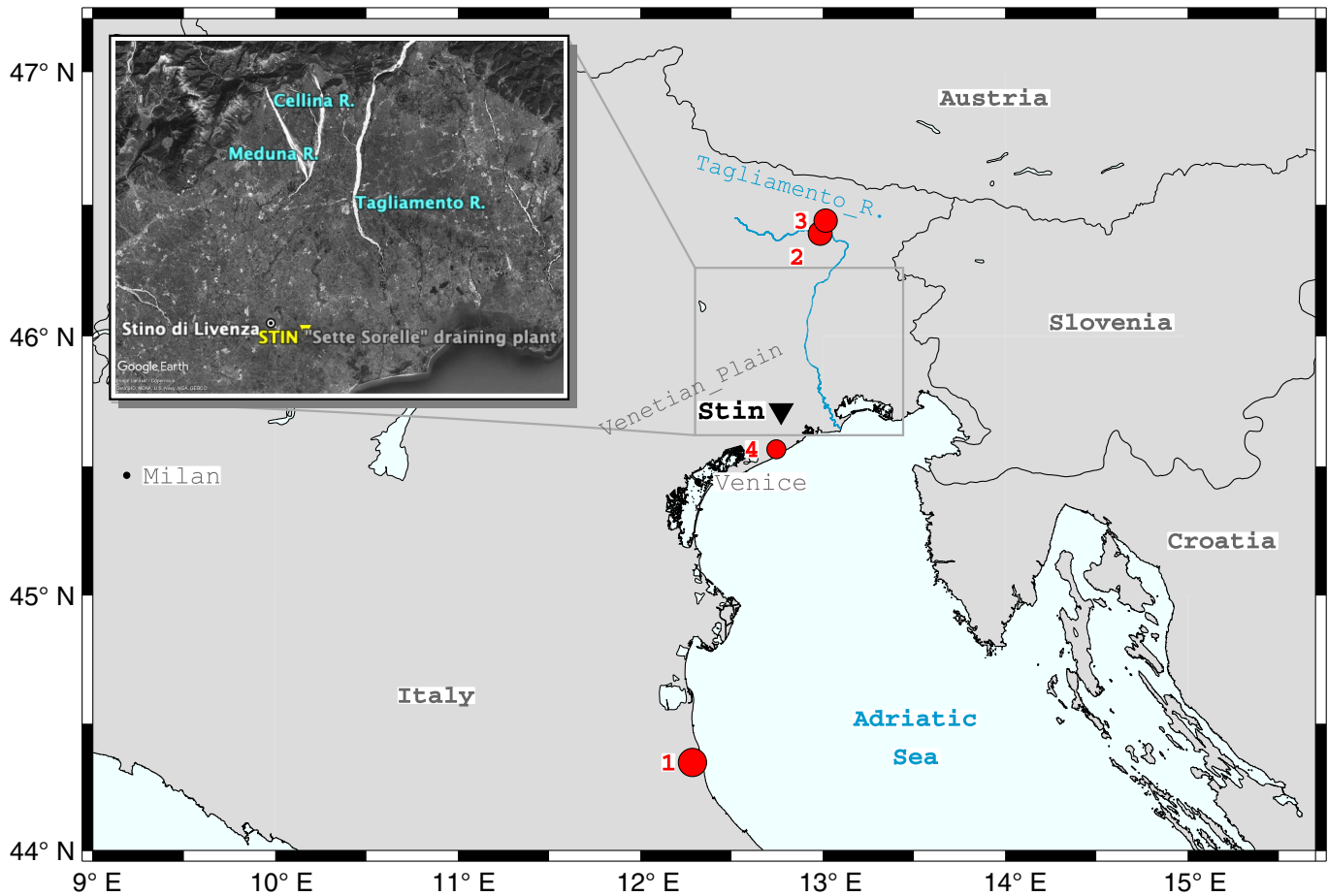
Methods
Inverting seismic noise array data

The processing of seismic noise data was carried out in two stages. First, a modified version of the extended spatial autocorrelation technique (Ohori *et al.*, 2002) was used to calculate the frequency-dependent Rayleigh-wave attenuation coefficients. The V_S profile was then obtained from the inversion based on Parolai *et al.* (2005), using the modified genetic algorithm suggested by Yamanaka and Ishida (1996). Second, a linear inversion was conducted to estimate the Q_S values, here assumed to be frequency independent, by inverting the attenuation coefficients constraining V_S to the values previously computed using SART. For a detailed description of the procedure, refer to Dreossi and Parolai (2022).

Inverting weak-motion recordings from the STIN borehole

The weak-motion data were analyzed using the deconvolution method in the spectral domain, as described by Mehta *et al.* (2007) and Parolai *et al.* (2009). The spectral deconvolution of the seismogram recorded at a depth of 100 m in the STIN borehole was carried out using the signal recorded at the surface as a reference (Parolai *et al.*, 2012), following the Tikhonov regularization approach to stabilize the deconvolution (Tikhonov and Arsenin, 1977). This method assisted in mitigating the effect of numerical instabilities resulting from
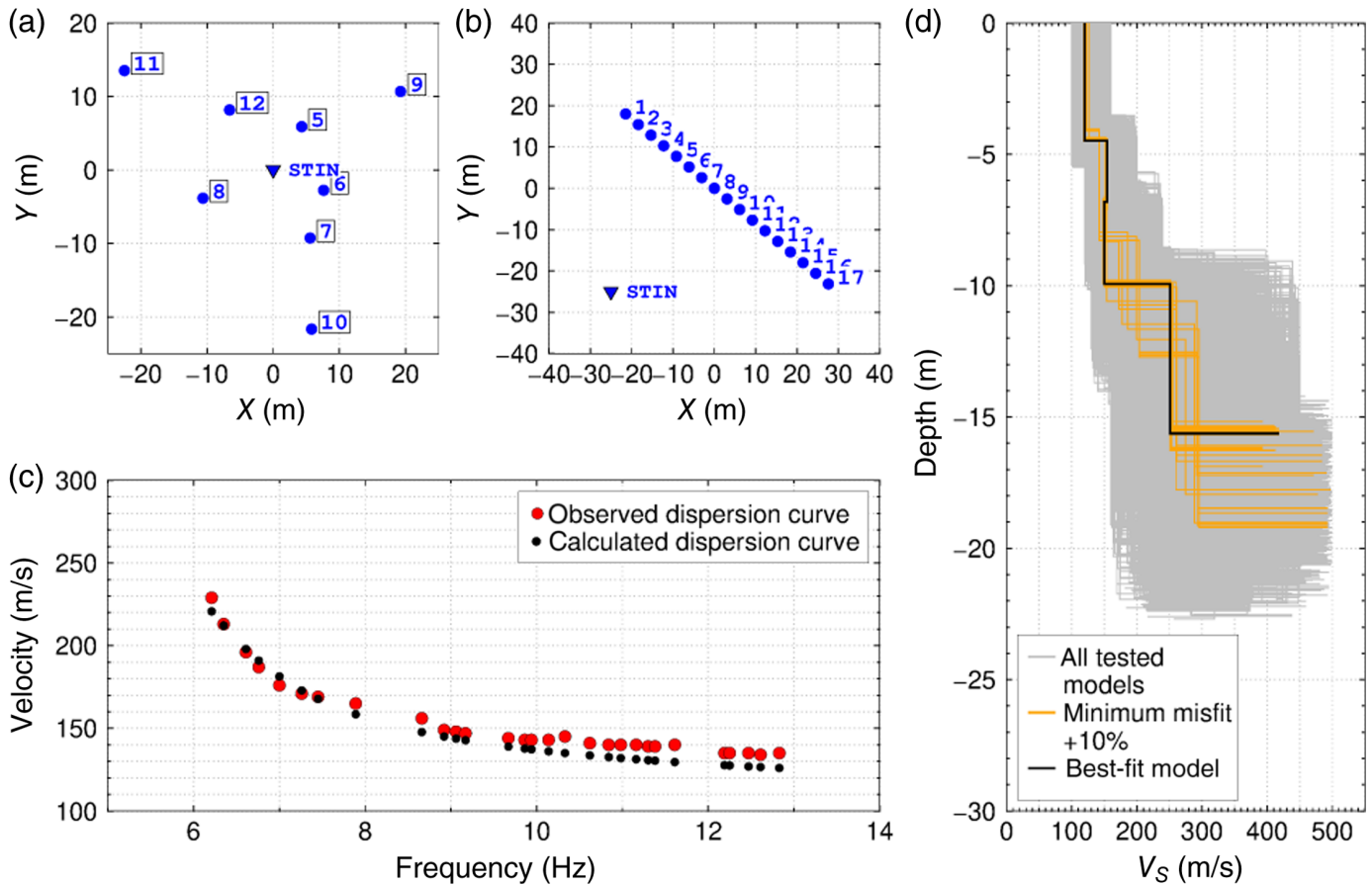
Figure 1. Map of the study area in northeast Italy. The STIN borehole station is marked with a black inverted triangle, and the four weak-motion events analyzed are represented by numbered red circles. The diameter of the red circles scales with increasing magnitude (range 3.1–4.6). In the upper-left corner (inset) of the figure is an enlarged view of the Google Earth satellite image showing the STIN borehole (indicated with a yellow inverted triangle) location and a portion of the plain to the left and right of the Tagliamento River.

reliance on the use of the spectral ratio (e.g., Parolai *et al.*, 2010). A forward modeling of the wavefield was undertaken, starting from a 1D borehole input model, and was repeated at every step of the inversion process. After obtaining the synthetic seismogram at the bottom using Wang (1999) viscoelastic matrix propagator method, which estimates the *P*, *SV*, and *SH* wavefields, the synthetic Green's function and fast Fourier transform (FFT) were computed. Then, the deconvolved synthetic spectrum of the sensor at the bottom was retrieved. The deconvolved wavefield of synthetic data was used to compute the residuals with the observed deconvolved wavefield, which is the target of the inversion procedure. The singular value decomposition algorithm (Press *et al.*, 1986) was utilized to solve the linear system. The model underwent several adjustments until the root mean square (rms) of the difference between the observed and synthetic inverse spectral amplitudes of the Green's function was reduced and a satisfactory convergence of the solution was achieved. The inversion process was run for 40 iterations.

Data

In the first part of the study, a seismic noise measurement campaign was conducted in array configuration surrounding the STIN borehole. The campaign involved eight stations, which were each equipped with a 1 Hz three-component velocimetric sensor (Lennartz 3D-lite), a datalogger set with a sampling rate of 100 Hz, a Global Positioning System antenna, and a battery. These stations were positioned on the ground to follow two approximately concentric circles with diameters of 19 and 45 m, respectively (Fig. 2a). They recorded data simultaneously for two hours at a sampling frequency of 250 samples/s. The

Figure 2. V_S inversion results obtained through analysis of the apparent Rayleigh-wave dispersion curve. (a) The seismic noise array geometry, and (b) the seismic noise recording obtained through the multichannel analysis of surface waves (MASW) configuration. (c) Observed dispersion curve (red circles) and the calculated Rayleigh-wave dispersion curve (black circles). (d) 1D V_S profiles. The figure shows the best-fit model (black line), along with models within 10% of the best-fit model (orange lines), and all tested models (gray lines).

minimum and maximum distances between stations were about 7 and 45 m, respectively. Field acquisition procedures based on MASW were carried out about 30 m east of the STIN borehole, deploying 17 4.5 Hz vertical single-component geophones arranged linearly with an interstation distance of 4 m (Fig. 2b). An ∼20-minute seismic noise acquisition was also performed using the MASW configuration prior to the eight-station passive-source array. Only the seismic noise acquisition derived from the MASW layout was considered in this study, since the work is based on seismic noise array analyses. The vertical-component record of each station was divided into nonoverlapping 60 s windows, and each window was tapered for 5% of its length at both the ends with a cosine function to minimize leakages. The spatial correlation coefficients were then computed and subsequently inverted to yield the 1D Q_S profile.

The second part of the study involved examining four weak-motion seismic recordings from the two seismometers installed in the STIN borehole (Fig. 1. For a list of events, see Table S2). They were subjected to an instrumental correction to allow comparison between the traces recorded by the velocimeter and those recorded by the accelerometer, and the velocimetric components were considered for the calculation. Initially, the trace of the sensor at the bottom was aligned with the north of the trace of the sensor at the top after the rotation angle was obtained by low-pass filtering (corner frequency 0.4 Hz) of both traces. Second, the horizontal components of each sensor were rotated in the direction displaying the highest spectral energy to maximize the similarity between the two components. Third, the arrival window for the shear (S) wave was selected, and the most energetic component of the horizontal S-wave phase was processed. This included computing the FFT, followed by processing the deconvolved traces and related
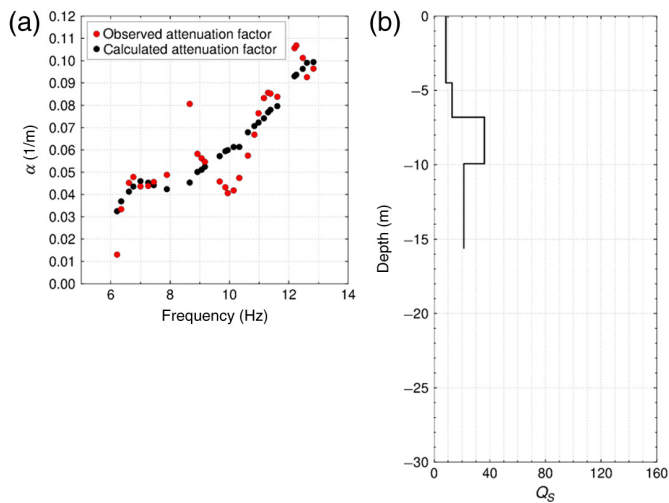
Figure 3. Q_S inversion results. (a) Observed attenuation factors (red circles) and retrieved attenuation factors (black circles). (b) 1D Q_S profile (black line) obtained by initially setting the attenuation value to 0 using $\lambda = 0.4$; based on 30 simultaneous algebraic reconstruction technique (SART) iterations.

spectra and calculating the inverse FFT. Fourth, the resulting traces were stacked together to produce a single deconvolved spectrum.

Results

Seismic noise array data

The apparent Rayleigh-wave phase velocity dispersion curve retrieved by the array (in the frequency range 6.2–7.9 Hz) and the MASW (8.7–12.8 Hz) was inverted. The usable bandwidth was limited by both the seismic noise measurement array aperture and the mechanical properties of the test site soils.

Four independent inversions were run using four seed numbers for the genetic algorithm inversion, with a starting population of 50 models that iterated for 100 generations. The mutation rate, which maintains diversity in the population, was fixed at 0.01. The crossover rate, which randomly combines favorable features of two or more selected parent models, was set at 0.7. The values of both operators are consistent with the values indicated by Parolai *et al.* (2006). The optimal 1D V_S model was chosen based on the minimum misfit, specifically the lowest average rms deviation between the observed and theoretical data of all generated models. Figure 2c,d illustrates the results of the V_S inversion.

Assessment of Q_S, the parameter of focus in this article, was performed on the first four layers of the best 1D V_S model.

This is because the Jacobian matrix of the partial derivatives of V_S (or data kernel matrix) and the model resolution matrix (not depicted here) at depths greater than 15.6 m, estimated by linearizing the problem, showed poor sensitivity to the quality factor of the attenuation curve. The solution was deemed satisfactory after conducting 30 SART iterations. Based on Dreossi and Parolai (2022), the starting value of the attenuation was configured to 0, and no attenuation positivity constraint was set. The relaxation parameter λ used to slow down the convergence rate of the solution while avoiding noise increase was set to a value of 0.4. In fact, values of λ less than 1 make the solution converge progressively and reduce the noise in the solution (e.g., Sweeney and Vest, 1973; Andersen and Kak, 1984). Figure 3a displays the retrieved attenuation factor, which succeeds in capturing the general trend of the function. Figure 3b presents the 1D Q_S model acquired through seismic noise analysis, with a Q_S value of ~15.

Weak-motion recordings from the STIN borehole

After processing the four weak-motion events, as described in the Data section, the respective Green's functions in the time domain were stacked together to improve the signal-to-noise ratio (see Fig. 4a). Then, the Green's function spectrum at 100 m depth was calculated (Fig. 4b). Following this step, the linear inversion was performed in the frequency band of 0.6–3.1 Hz. The frequency band considered was approximately the interval in which the autocorrelation of the surface (reference) sensor spectrum did not decay.

A two-layer model was adopted for the inversion process. This choice, in apparent discrepancy with the four-layer model derived from the surface array-based seismic noise analysis, is related to the number of seismometers installed in the STIN well. In fact, because there are only two sensors, the velocity in a number of layers greater than two (as would be the case here) could be justified by different models due to the limited frequency band that can be exploited, as long as they can represent the average velocity. Diverse independent input models were tested. In all of them, the first layer contained the average V_S and Q_S values, in terms of travel time, from the 1D four-layer model obtained from the seismic noise processing. The values for thickness, V_S, and Q_S were, respectively, set to 15.6 m, 163 m/s (i.e., the average V_S estimated at a thickness of 15.6 m), and ~15 (i.e., the average Q_S retrieved at a thickness of 15.6 m). These values were considered reliable in describing the subsoil closest to the surface. For the second layer, the thickness was fixed at 114.4 m and V_S set to
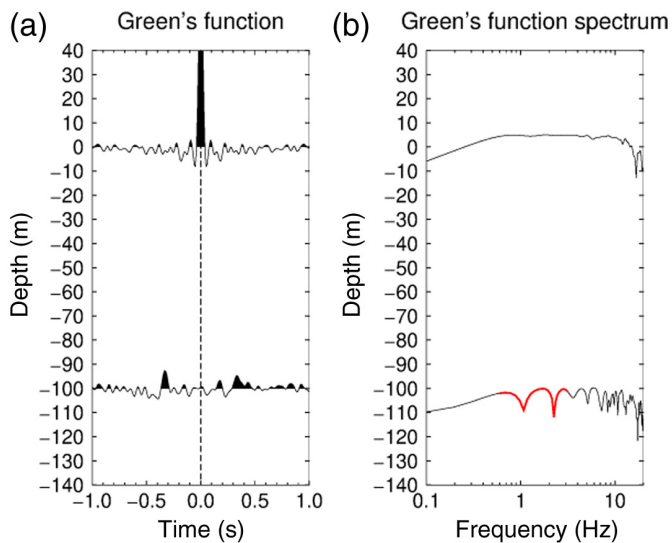
Figure 4. (a) The Green's function shown is the deconvolved wavefield (measurement unit: s^{-1}) obtained by stacking the four weak-motion events. The time window adopted is 2 s, and it is centered on 0 s. (b) The Green's function spectra, which denote the amplitude spectra of the deconvolved wavefield at depths between 0.5 and 100 m, are displayed in a logarithmic scale. The analysis is confined to the red-colored frequency range.

430 m/s by the average STIN borehole stratigraphy. The initial Q_S in the second layer ranged from 80 to 500, depending on the initial model used, to investigate how well the final 1D Q_S model was constrained.

Figure 5 displays the outcomes from four inversions highlighting the variability in the obtained Q_S values. In Figure 5a, a comparison is made between the input spectrum of the deconvolved wavefield and the output spectra of the deconvolved wavefield for the final 1D models of the inversion. Note that each data value represents a frequency analyzed. The analyses highlight that the fit between the input spectrum and the output spectra is good only up to the first spectral peak. When examining a data value larger than 26, which corresponds to the frequency of 3.1 Hz, certain ranges show identical results in final models, and others reveal divergent responses. The final 1D V_S models are consistent with each other, as indicated in Figure 5b. The first layer of the final 1D Q_S model also displays fairly consistent results among the tested cases, as shown in Figure 5c. On the contrary, Q_S in the second layer cannot be accurately determined. In fact, the model resolution matrix (not shown here) did not predict Q_S in the second layer for almost none of the initial Q_S values tested. However, models with a lower initial Q_S value in the second layer seem to better

justify the spectral peaks. The final 1D V_S and Q_S models obtained by setting an initial Q_S value of 200 match the average results of the seismic noise analysis discretely well. The final V_S values are 130 m/s for the first layer and 456 m/s for the second layer. The corresponding final Q_S values are 55 and 193 for the first and second layers, respectively. Figure 5d compares the 1D Q_S model resulting from the surface array-based seismic noise analysis with that derived from the borehole weak-motion recordings using an initial Q_S of 200.

Discussion and Conclusions

In this study, the Q_S parameter was estimated at the local scale using seismic noise data gathered in an array configuration at the STIN borehole site. The linear inversion method based on the SART algorithm developed by Dreossi and Parolai (2022) was employed for the estimation. The aim was to compare the Q_S obtained using this method with the Q_S retrieved by analyzing weak-motion events recorded by two sensors permanently located at the top and bottom of the STIN well. The analysis assumes that the Q_S calculated from weak-motion data inversion is reliable and can be compared to the one obtained from seismic noise. Hence, if the two Q_S values are similar, it may indicate the feasibility of adopting the seismic noise technique used here to assess Q_S for local seismic site evaluations in urban environments quickly and efficiently.

The V_S and Q_S values gained from the array configuration at the top of the STIN borehole were limited to the first tens of meters of depth. Despite considering an aperture of about 45 m suitable to investigate a depth of up to 40 m by means of the seismic noise array, it was found to be inadequate for the STIN location. This could be due to local lateral transitions that occur suddenly in this area of the plain, which are associated with detectable paleochannels (e.g., Bondesan *et al.*, 2011) that may show strong density differences among gravels, sands, and peat. As a consequence, supported results of both V_S and Q_S are available only down to a depth of 15.6 m.

Weak-motion record analyses in the STIN borehole yielded V_S values consistent with the array V_S for the first 15.6 m depth (layer 1). Also for the 15.6–114.4 m depth range (layer 2), V_S was consistent with the STIN borehole stratigraphy, although not very well constrained for models with high initial Q_S in layer 2. On the other hand, the Q_S value in the first 15.6 m depth (layer 1) was discretely constrained. In the 15.6–114.4 m depth range (layer 2), instead, the Q_S values cannot be resolved due to lack of resolution.
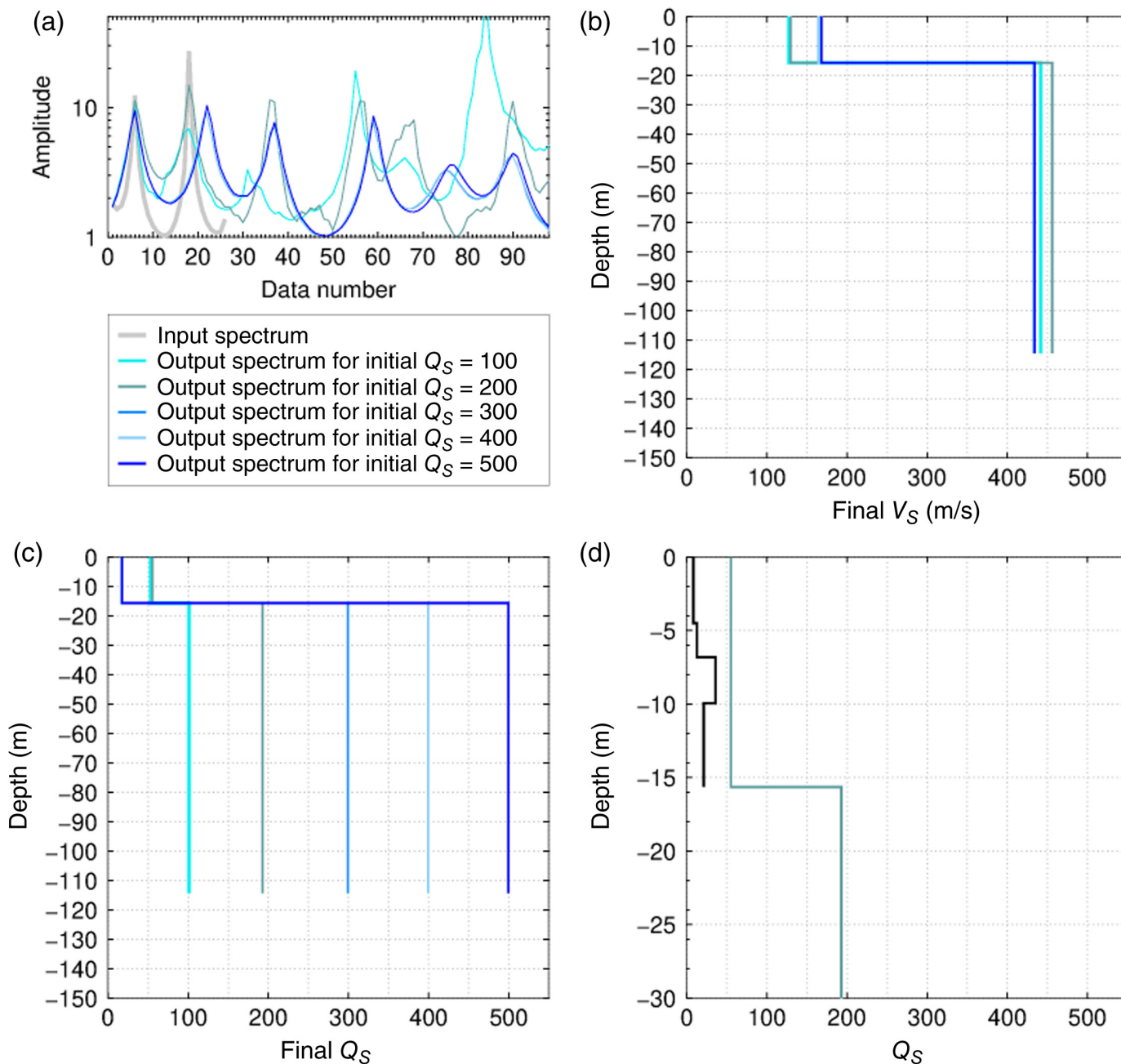
Figure 5. (a) The input spectrum of the deconvolved wavefield (gray line) and the output spectra of the deconvolved wavefield for the final inversion models generated by testing input setup models with different Q_S values (colored with different shades of blue). Each data number between 0 and 26 represents an analyzed frequency of the input deconvolved spectrum (0.6–3.1 Hz). The output spectra at frequencies higher than those included in the deconvolved input spectrum are also included between data numbers 27 and 100 to provide an overview of the resulting spectra. (b) Final 1D V_S models obtained using the stacked spectrum of the four weak-motion events in the frequency range of 0.6–3.1 Hz as the input spectrum for the deconvolved wavefield. The various input setup models are reported with their corresponding colors, which are visible in panel (a). (c) Final 1D Q_S models estimated from the same input models used in panels (a) and (b). (d) Comparison between the 1D Q_S model obtained from the surface array-based seismic noise technique (black line) and the 1D Q_S model resulting from the weak-motion data analysis using an initial Q_S value of 200 (cadet blue line). In general, a systematic difference was observed in the 0–15.6 m depth range between the mean Q_S estimated from surface array-based seismic noise and the Q_S from weak-motion recordings.

The V_S estimated in this study is consistent with that of other independent studies conducted in an alluvial context (e.g., Foti et al., 2011; Boxberger, 2016). Regarding Q_S, the two methods converge in determining a value of the same order or magnitude for the first 15.6 m depth. The discrepancy between the differently estimated Q_S may be related to the inadequacy of the surface wave-based method in an area such as the one considered or even to the fact that the number of inverted weak-motion events (i.e., 4) is small. However, the Q_S results are consistent with values found at other Italian and non-Italian research sites (e.g., Boxberger, 2016). At greater depth, a Q_S of ∼190 might be expected, considering input models with an initial Q_S of about 200, where the spectral peaks are better accounted for. In the context of unconsolidated alluvial sediments, a Q_S value of about 190 at depth is a plausible result when considering the Q_S estimated at a test site by Boxberger (2016) in the 20–70 m depth range.

The outcomes indicate that the technique adopted for inverting seismic noise data in an array configuration can provide favorable results in less geologically complex contexts that adhere to 1D site conditions. To further explore Q_S at STIN, a surface seismic noise survey using a new array geometry and greater spatial aperture would be beneficial in reaching greater depths. In particular, the geometry could be varied to reduce the aliasing effect and configured to cover a wide range of directions and distances. Although the resolving power may be reduced due to seismic heterogeneities within or near the array, a larger spatial aperture would allow longer wavelengths to be recorded, thus extending the frequency bandwidth for dispersion modeling to lower frequencies. Moreover, installing additional sensors at varying depths within the STIN well would provide a more comprehensive 1D Q_S profile from weak-motion records, specifically down to a depth of 100 m. More stable results may also be obtained by having more weak-motion events available.

Data and Resources

Data used in this article are available at https://opendata.ogs.it/STIN_experiment_2021_2022/. The website to the National Institute of Oceanography and Applied Geophysics—OGS web platform for performing joint inversions based on Parolai et al. (2005) (available to everyone after free registration) is http://joinv.crs.inogs.it/test/loginv-sec/index.php.

Figures were made using the Generic Mapping Tools (GMT) version 5.4.4 (https://www.generic-mapping-tools.org; Wessel et al., 2013). The free 3D graphics software Google Earth was utilized to zoom in Figure 1. All websites were last accessed in March 2024. The supplemental material contains two tables: Table S1, which shows the stratigraphy of the STIN borehole, and Table S2, which lists the four borehole weak-motion events analyzed in this paper.

Declaration of Competing Interests

The authors acknowledge that there are no conflicts of interest recorded.

Acknowledgments

References

Aimar, M., S. Foti, and B. R. Cox (2024). Novel techniques for in situ estimation of shear-wave velocity and damping ratio through MASW testing–I: A beamforming procedure for extracting Rayleigh-wave phase velocity and phase attenuation, Geophys. J. Int. 237, no. 1, 506–524, doi: 10.1093/gji/ggae051.

Andersen, A. H., and A. C. Kak (1984). Simultaneous algebraic reconstruction technique (SART): A superior implementation of the ART algorithm, Ultrason. Imag. 6, no. 1, 81–94, doi: 10.1016/0161-7346(84)90008-7.

Badsar, S. A., M. Scheveneels, W. Haegeman, and G. Degrande (2010). Determination of the material damping ratio in the soil from SASW tests using the half-power bandwidth method, Geophys. J. Int. 182, no. 3, 1493–1508, doi: 10.1111/j.1365-246X.2010.04690.x.

Bondesan, A., A. Fontana, P. Mozzi, S. Primon, V. Bassan, and A. Vitturi (2011). Atlante Geologico della provincia di Venezia. Note illustrative, Arti Grafiche Venete, 8, 333–366 (in Italian).

Boxberger, T. (2016). A comparison of different seismological and geotechnical parameters for site characterization, *Genehmigte Dissertation*, Technische Universität, Berlin, Germany.

Boxberger, T., M. Pilz, and S. Parolai (2017). Shear wave velocity versus quality factor: Results from seismic noise recordings, *Geophys. J. Int.* **210,** no. 1, 660–670, doi: 10.1093/gji/ggx161.

Bragato, P. L., P. Comelli, A. Saraò, D. Zuliani, L. Moratto, V. Poggi, G. Rossi, C. Scaini, M. Sugan, C. Barnaba, *et al.* (2021). The OGS–Northeastern Italy seismic and deformation network: Current status and outlook, *Seismol. Res. Lett.* **92,** no. 3, 1704–1716, doi: 10.1785/0220200372.

Dreossi, I., and S. Parolai (2022). Robust estimation of 1D shear-wave quality factor profiles for site response analysis using seismic noise, *Soil Dynam. Earthq. Eng.* **161,** 107387, doi: 10.1016/j.soildyn.2022.107387.

Fontana, A., A. Bondesan, M. Meneghel, F. Toffoletto, A. Vitturi, and V. Bassan (2012). Note illustrative della Carta Geologica d'Italia alla scala 1:50000, *Foglio 107—Portogruaro, Regione del Veneto, ISPRA, Roma, InfoCartoGrafica*, Piacenza (in Italian).

Fontana, A., P. Mozzi, and A. Bondesan (2010). Late pleistocene evolution of the Venetian–Friulian Plain, *Rend. Fis. Acc. Lincei* **21,** no. Suppl. 1, 181–196, doi: 10.1007/s12210-010-0093-1.

Foti, S., S. Parolai, P. Bergamo, G. Di Giulio, M. Maraschini, G. Milana, M. Picozzi, and R. Puglia (2011). Surface wave surveys for seismic site characterization of accelerometric stations in ITACA, *Bull. Earthq. Eng.* **9,** 1797–1820, doi: 10.1007/s10518-011-9306-y.

Koedel, U., and L. Karl (2020). Determination of the damping ratio by multi-channel spectral analysis of seismic downhole data, *Soil. Dynam. Earthq. Eng.* **136,** 106235, doi: 10.1016/j.soildyn.2020.106235.

Lai, C. G., and A. G. Özcebe (2016a). Causal damping ratio spectra and dispersion functions in geomaterials from the exact solution of Kramers-Kronig equations of viscoelasticity, in *Continuous Media with Microstructure 2*, B. Albers and M. Kuczma (Editors), Springer, Cham, doi: 10.1007/978-3-319-28241-1_24.

Lai, C. G., and A. G. Özcebe (2016b). Non-conventional lab and field methods for measuring frequency-dependent low-strain parameters of soil dynamic behavior, *Soil. Dynam. Earthq. Eng.* **91,** 72–86, doi: 10.1016/j.soildyn.2016.09.007.

Mehta, K., R. Snieder, and V. Graizer (2007). Downhole receiver function: A case study, *Bull. Seismol. Soc. Am.* **97,** no. 5, 1396–1403, doi: 10.1785/0120060256.

Ohori, M., A. Nobata, and K. Wakamatsu (2002). A comparison of ESAC and FK methods of estimating phase velocity using arbitrarily shaped microtremor arrays, *Bull. Seismol. Soc. Am.* **92,** no. 6, 2323–2332, doi: 10.1785/0119980109.

Parolai, S. (2014). Shear wave quality factor Q_S profiling using seismic noise data from microarrays, *J. Seismol.* **18,** 695–704, doi: 10.1007/s10950-014-9440-5.

Parolai, S., A. Ansal, A. Kurtulus, A. Strollo, R. Wang, and J. Zschau (2009). The Ataköy vertical array (Turkey): Insights into seismic wave propagation in the shallow-most crustal layers by waveform deconvolution, *Geophys. J. Int.* **178,** no. 3, 1649–1662, doi: 10.1111/j.1365-246X.2009.04257.x.

Parolai, S., D. Bindi, A. Ansal, A. Kurtulus, A. Strollo, and J. Zschau (2010). Determination of shallow S-wave attenuation by down-hole waveform deconvolution: A case study in Istanbul (Turkey), *Geophys. J. Int.* **181,** no. 1, 1147–1158, doi: 10.1111/j.1365-246X.2010.04567.x.

Parolai, S., C. G. Lai, I. Dreossi, O.-J. Ktenidou, and A. Yong (2022). A review of near-surface Q_S estimation methods using active and passive sources, *J. Seismol.* **26,** 823–862, doi: 10.1007/s10950-021-10066-5.

Parolai, S., M. Picozzi, S. M. Richwalski, and C. Milkereit (2005). Joint inversion of phase velocity dispersion and H/V ratio curves from seismic noise recordings using a genetic algorithm, considering higher modes, *Geophys. Res. Lett.* **32,** L01303, doi: 10.1029/2004GL021115.

Parolai, S., S. M. Richwalski, C. Milkereit, and D. Fäh (2006). S-wave velocity profiles for earthquake engineering purposes for the Cologne area (Germany), *Bull. Earthq. Eng.* **4,** 65–94, doi: 10.1007/s10518-005-5758-2.

Parolai, S., R. Wang, and D. Bindi (2012). Inversion of borehole weak motion records observed in Istanbul (Turkey), *Geophys. J. Int.* **188,** no. 1, 535–548, doi: 10.1111/j.1365-246X.2011.05252.x.

Press, W. H., S. A. Teukolsky, W. T. Vetterling, and B. P. Flannery (1986). *Numerical Recipes in Fortran 77, The Art of Scientific Computing*, Cambridge University Press, Cambridge.

Riga, E., F. Hollender, Z. Roumelioti, P.-Y. Bard, and K. Pitilakis (2019). Assessing the applicability of deconvolution of borehole records for determining near-surface shear-wave attenuation, *Bull. Seismol. Soc. Am.* **109,** no. 1, 621–635, doi: 10.1785/0120180298.

Ronchi, L., A. Fontana, K. M. Cohen, and E. Stouthamer (2021). Late Quaternary landscape evolution of the buried incised valley of Concordia Sagittaria (Tagliamento River, NE Italy): A reconstruction of incision and transgression, *Geomorphology* **373,** 107509, doi: 10.1016/j.geomorph.2020.107509.

Sweeney, D. W., and C. M. Vest (1973). Reconstruction of three-dimensional refractive index fields from multidirectional interferometric data, *Appl. Opt.* **12,** no. 11, 2649–2664, doi: 10.1364/AO.12.002649.

Tikhonov, A. N., and V. Y. Arsenin (1977). *Solution of Ill-Posed Problems*, Wiston/Wiley, Washington, D.C.

Wang, R. (1999). A simple orthonormalization method for stable and efficient computation of Green's functions, *Bull. Seismol. Soc. Am.* **89,** no. 3, 733–741, doi: 10.1785/BSSA0890030733.

Wessel, P., W. H. F. Smith, R. Scharroo, J. Luis, and F. Wobbe (2013). Generic Mapping Tools: Improved version released, *Eos. Trans. AGU* **94,** no. 45, 409–410, doi: 10.1002/2013EO450001.

Yamanaka, H., and H. Ishida (1996). Application of genetic algorithms to an inversion of surface-wave dispersion data, *Bull. Seismol. Soc. Am.* **86,** no. 1, 436–444, doi: 10.1785/BSSA0860020436.